Low Reynolds Number Airfoil Evaluation for the Mars Helicopter Rotor

Witold J. F. Koning
Aerospace Engineer
Science and Technology Corporation
NASA Ames Research Center
Moffett Field, California

Ethan A. Romander
Aerospace Engineer
NASA Ames Research Center
Moffett Field, California

Wayne Johnson
Aerospace Engineer
NASA Ames Research Center
Moffett Field, California

ABSTRACT

The present research provides a performance comparison between several low Reynolds number airfoil profiles for the Mars Helicopter. The low density of the Martian atmosphere and the relatively small Mars Helicopter rotor result in very low chord-based Reynolds number flows, $Re_c = O(10^3 - 10^4)$. At low Reynolds numbers, flat and cambered plates can outperform conventional airfoils, making them of interest for the Mars Helicopter rotor. Performance models are generated for the Mars Helicopter rotor based on a free wake analysis, and the results are compared with Mars Helicopter isolated rotor performance from previous work. A Reynolds-Averaged Navier-Stokes based approach is used to generate the airfoil deck using OVERFLOW. The model is constructed using airfoil data tables (C81 files) that are used by the comprehensive rotor analysis code CAMRADII. Performance results for the Martian atmosphere show improved performance for the cambered plate rotor over conventional airfoils, in terms of thrust for equal power and Figure of Merit for equal blade loading. The cambered flat plate airfoil produces 7% larger maximum rotor thrust versus the Mars Helicopter airfoils, and 5% larger Figure of Merit over the design thrust coefficient range. Larger maximum thrust allows an increase of design blade loading for the same thrust range for control authority, whereas the larger Figure of Merit reduces power requirements.

NOTATION

c	airfoil chord
c_d	section drag coefficient
c_l	section lift coefficient
c_m	section moment coefficient
C_T	thrust coefficient
f	airfoil camber
g	gravitational acceleration
M	Mach number
n	amplification factor
p	pressure
R	gas constant; rotor radius
r	rotor radial coordinate
Re	Reynolds number
Re_c	chord-based Reynolds number
Re_{δ^*}	displacement thickness Reynolds number
$Re_{\theta t}$	displacement thickness Reynolds number at transition
t	airfoil thickness
T	absolute temperature
x	airfoil x-coordinate
x_{ls}	x-coordinate of laminar separation
α	angle of attack
γ	specific heat ratio; intermittency
μ	dynamic viscosity
ρ	density
σ	standard deviation; rotor solidity
AFT	Amplification Factor Transport
APL	Johns Hopkins University Applied Physics Laboratory

Presented at the AHS International 74th Annual Forum & Technology Display, Phoenix, Arizona, USA, May 14-17, 2018.

AR	Aspect Ratio
BDF2	Backward Difference Formula (2nd order)
BL	Boundary Layer
CFD	Computational Fluid Dynamics
CO_2	Carbon Dioxide
DNS	Direct Numerical Simulation
FM	Figure of Merit
JPL	Jet Propulsion Laboratory
KH	Kelvin-Helmholtz
LES	Large Eddy Simulation
LEV	Leading Edge Vortex
LSB	Laminar Separation Bubble
MAV	Micro Aerial Vehicles
MC	Mars Condition
MH	Mars Helicopter
PIV	Particle Image Velocimetry
RANS	Reynolds-Averaged Navier-Stokes
SA	Spalart-Allmaras
SLS	Sea Level Standard
TI	Turbulence Intensity
TS	Tollmien-Schlichting
UAV	Unmanned Aerial Vehicle
VTOL	Vertical Take-Off and Landing

INTRODUCTION

Advances in the fields of electronics, batteries, and electric motors have enabled broad adoption of small-scale aircraft for various terrestrial applications. Numerous Micro Aerial Vehicles (MAVs) and small Unmanned Aerial Vehicles (UAVs), both civil and military, are in use today. Operation at their design flight condition often requires rotors, propellers, or wings to perform at Reynolds numbers significantly below 500,000. The chord-based Reynolds number for these small-scale rotors usually requires knowledge of airfoil performance at even lower Reynolds numbers.

The use of rotary wing UAVs for aerial mobility for planetary exploration has been studied lately [1], [2], notably the designs for the exploration of Mars and Titan by the Jet Propulsion Laboratory (JPL) Mars Helicopter (MH) [3] and the Dragonfly by Johns Hopkins University Applied Physics Laboratory (APL) [4], respectively. Both these vehicles have the unique ability, amongst others, to cover the resolution gap between orbiters and ground based rovers. The present work will compare several airfoils for the very low Reynolds number regime of the JPL MH. The chord-based Reynolds number distribution for the MH rotor covers from roughly $Re_c \approx 10^3$ to 10^4. The span wise Reynolds number distribution over the rotor is presented in Figure 1.

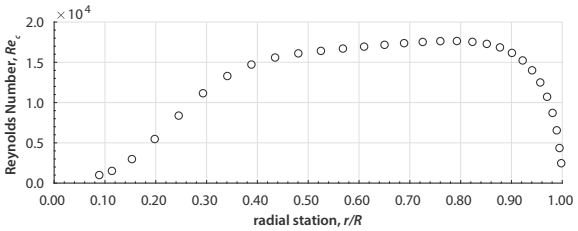

Figure 1. Approximate span wise Reynolds number distribution for the MH rotor in the Martian atmosphere (reproduced from Koning, Johnson, and Allan [7])

The NASA Jet Propulsion Laboratory designed the Mars Helicopter in collaboration with AeroVironment Inc., NASA Ames Research Center, and NASA Langley Research Center to explore the possibility of a Vertical Take-Off and Landing (VTOL) UAV for flight on Mars. The MH serves as a technology demonstrator, eventually intended to perform low-altitude flight in the Martian atmosphere.

The Martian environment provides major challenges for the design of the UAV. In 2014, Balaram and Tokumaru published an initial paper describing the conceptual design of the current Mars Helicopter [5]. More recently, Grip *et al.* published a paper describing the flight dynamics of the MH and experimental testing in the 25-ft. diameter Space Simulator at JPL [6]. Balaram *et al.* describe the key design features and results from a full-scale prototype [3].

The design of the MH is a solar powered co-axial helicopter with a mass of roughly 1.8 kg and a 1.21 m rotor diameter. The helicopter is battery powered allowing up to 90 s flight endurance that, because of the communication delay between Earth and Mars, will be conducted fully autonomously.

A prerequisite for satisfactory rotor performance is the proper design of the airfoil sections over the span. The very low Reynolds number regime is not well understood and little experimental and simulation work exists to date. The low lift-to-drag ratios of airfoils at very low Reynolds numbers only show that it is critical to understand the flow physics in order to maximize performance metrics [8]. The present work limits

itself to the investigation of two-dimensional airfoil flow physics and the subsequent characteristics for rotor performance prediction using comprehensive analyses. An identical twist and chord distribution to that of the MH rotor is used, and the original design is compared to flat plate and cambered plate airfoils to investigate low Reynolds number rotor performance. The rotor performance is compared to the performance estimation for the proposed MH rotor design, as analyzed by Koning, Johnson, and Allan [7].

LOW REYNOLDS NUMBER AIRFOIL AERODYNAMICS

At low Reynolds numbers the aerodynamic performance of airfoil sections drops. At a critical Reynolds number, flat and cambered plates can outperform smooth airfoils [9]–[15]. Figure 2 shows a summary of airfoil performance versus Reynolds number from McMasters and Henderson [10]. Performance of smooth airfoils drops rapidly as the Reynolds number is reduced below approximately $Re_c \approx 10^5$. The performance of a locust is included for reference in the figure as insects and birds tend to operate at very low Reynolds numbers.

McMasters and Henderson also present the minimum section drag versus Reynolds number, shown in Figure 3, which shows a rise in drag for smooth airfoils at the same critical Reynolds number. These figures demonstrate the need to evaluate flat or cambered plate airfoils for rotors in the chord-based Reynolds number range of the MH rotor.

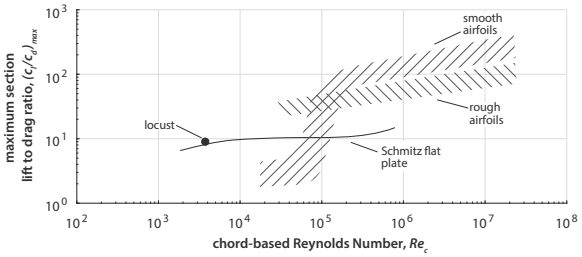

Figure 2. Maximum section lift to drag ratio versus Reynolds number (reproduced from McMasters and Henderson [10])

The substantial change in airfoil performance is related to boundary layer transition on the airfoil as a function of Reynolds number. At low Reynolds numbers the boundary layer can be fully laminar up to the point of separation without subsequent (turbulent) flow reattachment or on-body transition. The flow state is then called subcritical. The Reynolds number at which laminar flow over an airfoil just begins to exhibit turbulent features (either due to transition or turbulent reattachment) is called the critical Reynolds number; roughly the region at $Re_c \approx 10^5$ in Figure 2 and Figure 3. Reynolds numbers where turbulent transition always occurs before laminar separation or during/after reattachment are referred to as supercritical.

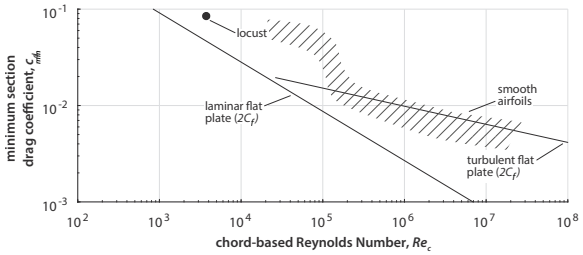

Figure 3. Minimum section drag coefficient versus Reynolds number (reproduced from McMasters and Henderson [10])

The critical Reynolds number is affected by the state of the boundary layer, which is primarily a function of the Reynolds number, section shape, lift coefficient, free stream turbulence, external disturbances, and surface roughness [9], [16].

LOW RE AIRFOIL PERFORMANCE

In the very low Reynolds number regime, the boundary layer can still be laminar after the point of pressure recovery. The laminar boundary layer is prone to separation as the adverse pressure gradient rises with increasing lift coefficient. Early separation causes large drag coefficients in subcritical flow (an order of magnitude higher than their supercritical counterparts, as shown in Figure 2).

The relatively thick boundary layer at low Reynolds numbers reduces the effective camber of the airfoil which in turn reduces the attainable lift coefficient, especially if a separated shear layer fails to reattach. Lift coefficients are not decreased to the same extent as the increase in section drag coefficient, resulting in low lift to drag ratios for airfoils in the subcritical flow state.

SEPARATION BUBBLES

The laminar separated shear layer is susceptible to transition, and can undergo rapid (in time or

space) transition to turbulent flow. The increased entrainment by the separated shear layer can lead to reattachment of the flow, creating a Laminar Separation Bubble (LSB) [16], [17]. The low velocities inside the bubble are linked to the characteristic flat pressure distribution of an LSB.

Periodic unsteadiness can be observed due to the unstable reattachment region caused by fluctuating entrainment of the fluid in the shear layer, periodic stabilization of the reverse-flow boundary layer, and possible developing eddy structures [18]. Movement of the bubble over the airfoil can therefore occur, as also observed by Gaster [19]. Pauley, Moin, and Reynolds [20] found the magnitude of the adverse pressure gradient to be the criterion for the onset of vortex shedding after laminar separation.

In addition to Tollmien-Schlichting (TS) instabilities, the shear layer flow is also observed to oscillate due to Kelvin-Helmholtz (KH) instabilities [18], which, if the flow does not reattach, could develop into KH vortices having an impact on fluctuating forces on the airfoil [17]. At high Mach numbers, possible shock-induced separation and transition cause additional complexities in the flow.

If an LSB occurs at the low Reynolds number, the level of freestream turbulence intensity can alter when (or if) reattachment occurs, and as such can strongly affect expected airfoil performance [13]. Angle of attack changes and boundary layer receptivity (the process by which free-stream disturbances influence or generate instabilities in the boundary layer) can greatly influence bubble formation [21] and thus airfoil performance [22] which is linked to the often significant hysteresis encountered in experimental low Reynolds number research around $Re_c \approx 10^5$ [9], [21].

On the other hand, continued reduction of the Reynolds number will cause the flow to fail to reattach, therefore not creating a closed LSB [16]. For helicopter rotors the boundary layer receptivity, angle of attack changes, and vibrations can change with flight condition and azimuthal location, thus making evaluation of LSBs very important at lower Reynolds numbers for rotor performance (and vibration) estimates.

Mueller and DeLaurier [23] state, after Carmichael [12], that for airfoils below $Re_c \approx 5.0 \cdot 10^4$ the free shear layer after laminar separation does not normally transition to turbulent flow in time to reattach to the airfoil surface. Lissaman [24] also observes complete laminar flow can occur for small angles of attack below $Re_c \approx 3 \cdot 10^4$, with boundary layer reattachment unlikely below $Re_c \approx 7 \cdot 10^4$.

Wang *et al.* [22] and Huang and Lin [25] investigated flow structures and characteristics of vortex shedding for an NACA 0012 airfoil. Eight distinct flow patterns were identified based on angle of attack and Reynolds number. Figure 4 shows the different flow structures and stall modes for the NACA 0012 airfoil, showing more modes than the classic leading edge stall, trailing edge stall, and thin-airfoil stall known for higher Reynolds number regimes [26], [27].

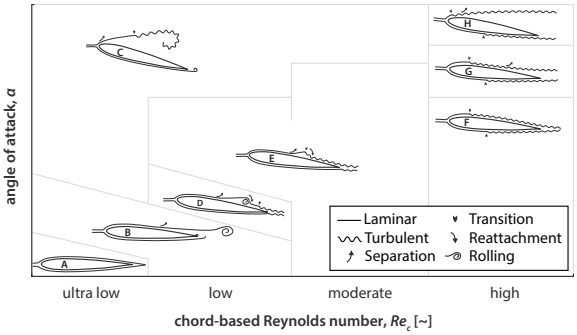

Figure 4. Schematic of flow structures around NACA 0012 airfoil for each Reynolds number regime (reproduced from Wang et al. [22])

A thorough investigation on vortex shedding at low Reynolds numbers was performed by Yarusevych, Sullivan, and Kawall [28].

LEADING EDGE VORTEX

The LSB can form a Leading Edge Vortex (LEV) when located at the leading edge and subjected to a sufficiently large axial flow component (high wing sweep and wing dynamics are the prime causes [29]). This cannot be captured using two-dimensional Computational Fluid Dynamics (CFD).

Helicopter rotors do not usually exhibit a large component of axial flow, although highly twisted blades can have span wise flows that substantially influence stall characteristics and

can cause stall delay. This makes a stable LEV unlikely for a conventional rotor and therefore no LEV-induced lift coefficient increases are expected to occur. With sufficient axial flow over the wing, the spiral LEV can occur, but only in the low Reynolds number regime at laminar Reynolds numbers; transition to turbulence has been observed to break the flow structure down to the usual two-dimensional instability [30]. At very low flight Reynolds numbers associated with the flapping wings of insects and birds, the LEV allows for relatively high lift coefficients.

CAMBERED AND FLAT PLATE PERFORMANCE

Flat plates, especially with sharp leading edges, behave differently at low Reynolds numbers than conventional airfoils. Hoerner [9] presents insight into differences in performance between a flat plate and airfoil crossing the critical Reynolds number transition region. The section lift and drag coefficient behaviors are shown in Figure 5 and Figure 6, respectively.

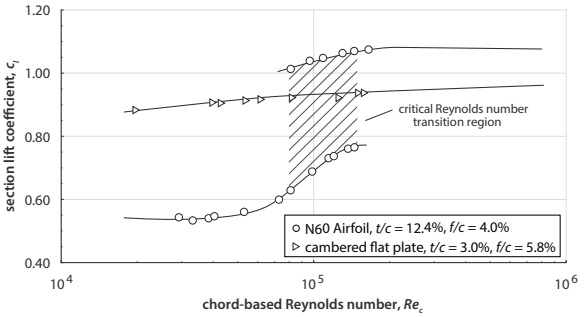

Figure 5. Variation of section lift coefficient with Reynolds number at constant angle of attack (reproduced from Hoerner [9])

The flat plates in the comparison have a thickness ratio of $t/c = 3.0\%$. A low thickness ratio has a beneficial effect on the drag coefficient [31], [32].

The sharper the leading edge, the earlier transition starts [11]. For all positive angles of attack, the stagnation point moves downstream on the lower surface, creating a turbulent edge, essentially forcing supercritical behavior up to very low Reynolds numbers. A sharp leading edge flat plate will therefore not exhibit a critical Reynolds number because the point of breakaway is fixed. The turbulent edge has both an immediate and a fixed transition location at all non-zero angles of attack [11]. Crompton indicates the high shear turbulent fluid feedback and natural KH instability as main reasons for rapid transition [18]. He found the transition to turbulence to be at $x/c \approx 2.5\%$ for flat plates at $Re_c \approx 10^4 - 10^5$ [18]. Schmitz [11] notes that beneficial turbulent reattachment occurs for flat plates up to angles of attack around $\alpha \approx 7° - 10°$, whereas Crompton indicates reattachment up to $\alpha \approx 5°$. Laitone [13] reports a similar range and observes for $Re_c < 4.0 \cdot 10^4$ and $\alpha < 8°$ that the large leading edge bubble (compared to blunt leading edges) is replaced by continuous shedding of small vortices over the upper surface, thereby mitigating the effects of total flow separation.

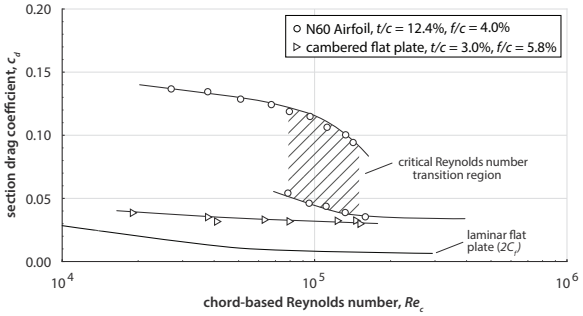

Figure 6. Variation of section drag coefficient with Reynolds number at constant angle of attack (reproduced from Hoerner [9])

Neither the trailing edge shape [13], [33], nor freestream turbulence levels [33], seem to impact cambered flat plate performance to any significance. No hysteresis occurs for thin flat plates, compared to that observed for thicker airfoils, because the nose turbulence increases faster than the pressure increase [11]. Okamoto *et al.*, Laitone, and Pelletier and Mueller show the comparatively low influence of freestream turbulence [13], [32], [33].

However, there must be a Reynolds number at which the flow does not transition to turbulence, despite the sharp leading edge. Indeed, flat plates at low Reynolds numbers around $Re_c \approx 10^4$ have been shown to have laminar flows without transition to turbulence [34], [35].

Camber usually has a positive effect on plate performance because of the low incidence angle between the freestream and the camber line at the leading edge. The turbulence generated by the sharp leading edge and the concave underside

both aid in lift generation, while sufficiently small upper surface camber allows largely attached flow [11].

The flow modes for the NACA 0012 as shown in Figure 4 are likely to have slightly different equivalents for flat plates. Mode B is unlikely to exist as separation is immediate from the leading edge. Mode A must exist, but it is not known over what Reynolds number range and what the dependency and influence of the sharp leading edge is. Flow modes C and D are combined as the flat plate will initially separate but can reattach (and possibly separate again). The cambered flat plate allows, on the contrary, most likely a separate flow mode B and D due to the camber of the upper surface.

Experimental results seem to contradict each other on whether turbulent reattachment of the separated shear layer from the leading edge of a flat plate indeed occurs. Laitone [13] does not mention an LSB, and Pelletier and Mueller [33] do not observe an LSB for (cambered) flat plates and airfoils around $Re_c \approx 10^4$. In the experimental work by Suwa *et al.* [36] and Anyoji *et al.* [37], [38], however, the existence of an LSB is deduced from the pressure distribution obtained via pressure sensitive paint observations for similar geometry and Reynolds numbers. Anyoji *et al.* found the flat plate reattachment state to disappear between $Re_c \approx 4.3 \cdot 10^3 - 1.1 \cdot 10^4$ [37]. It is unclear to what extent the evaluation of the flow field using time-accurate and time-averaged methods might skew observations as to the existence of an LSB.

Schmitz says $Re_c \approx 1.0 \cdot 10^4 - 2.0 \cdot 10^4$ is enough for sharp leading edge boundary layer transition [11]. Werle shows a flat plate at $\alpha \approx 2.5°$ and $Re_c \approx 1.0 \cdot 10^4$ with laminar reattachment, whereas at $Re_c \approx 5.0 \cdot 10^4$ the shear layer turns turbulent prior to reattachment [34], [35].

Using Direct Numerical Simulation (DNS) Sampaio, Rezende, and Nieckele [39] show the possibility of a secondary separation bubble. This bubble was also observed by Crompton [18] experimentally. A sketch of the separation bubble on a flat plate is provided in Figure 7.

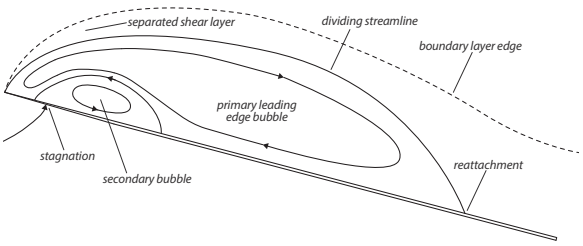

Figure 7. Sketch of laminar leading edge separation bubble (not to scale, created referring to Sampaio *et al.* [39])

When the reattachment point reaches the trailing edge, the bubble effectively 'bursts', which is likely to be periodic vortex shedding [11], [20].

MARS ATMOSPHERIC CONDITIONS

The low density Martian atmosphere and the relatively small MH rotor result in very low chord-based Reynolds number flows of around $Re_c \approx 1.5 \cdot 10^4$. Furthermore, the low density and low Reynolds number reduce the lifting force and lifting efficiency, respectively, which are only marginally compensated for at the vehicle level by a lower gravitational acceleration of approximately $g = 3.71\ m/s^2$.

The low density requires a high tip speed to generate thrust. However, the low temperature and largely CO_2-based atmosphere result in a low speed of sound, further constraining rotor operation in the Martian atmosphere by increasing compressibility effects [7].

Operation of the MH rotor in the Martian atmosphere occurs at a rare combination of high Mach and low Reynolds number. It is estimated that the Mach-Reynolds number combination results in a Knudsen number low enough for the flow to be considered a no-slip continuum [9].

JPL MARS HELICOPTER ROTOR PERFORMANCE

Koning *et al.* [7] generated an aerodynamic rotor model for comprehensive analyses for the JPL MH in hover. For very low Reynolds number flows turbulent transition is often pre-assumed. An approximate stability analysis using the e^n method of Smith and Gamberoni [40] and van Ingen [41] was performed using two-dimensional boundary layer analysis [42], [43] over the airfoils to estimate the transition likelihood in

combination with the stability charts by Wazzan *et al.* [44].

Even though the standard two-dimensional boundary layer approximation assumes a relatively thin boundary layer, comparisons between the boundary layer approximations, the thin-layer Reynolds-Averaged Navier-Stokes (RANS) approach, and a full RANS solution using OVERFLOW showed only small differences in laminar separation location and aerodynamic coefficients for the airfoils under consideration. In absence of test data, the minor differences were considered to be beyond the confidence in any of the results.

Tollmien-Schlichting (TS) waves were assumed to be the dominant transition-initiating mechanism. Beyond the instability limit (where amplification of disturbances first becomes possible), the amplification of TS waves in the BL was not sufficient to cause transition, with the cumulative amplification ratio, or transition parameter, n being extremely low at the point of laminar separation (the largest positive amplification rate calculated is $n \leq 1$ for the majority of airfoils). With normally used total amplification ratio values $4 < n < 14$ to account for various levels of freesteam turbulence, transition is still unlikely, unless bypass transition is the dominant transition mechanism. Dust, vibrations, and freestream turbulence all reduce the computed necessary amplification. Usually n is reduced to reflect those conditions. The conditions have to be very severe if n reduces from $n \approx 9$ down to $n \approx 1$.

The subsequent possibility of transition in the separated shear layer was ruled out through a combined interpretation of the Owen-Klanfer criterion [45] and Schubauer and Klebanoff's condition [46]. Schubauer and Klebanoff found that turbulent spots grow only very slowly for displacement thickness Reynolds numbers less than $Re_{\delta^*} \approx 450$. The Owen-Klanfer criterion predicts bubble type (long or short) based on the magnitude of Re_{δ^*}. Rapid transition becomes possible for a Reynolds number exceeding $Re_{\delta^*} \approx 450 - 500$. Crabtree [47], and later, Moore [48], interpreted the criterion as a condition for the growth of turbulent spots, thereby coinciding with the work by Schubauer and Klebanoff. This was summarized by Carmichael [12] stating that a Laminar Separation Bubble (LSB) for a Reynolds number with laminar separation below $Re_{\delta^*} \approx 500$, is unlikely.

The analysis of the Mars Helicopter airfoils [7], [49] showed average displacement thickness Reynolds numbers at the point of laminar separation of $Re_{\delta^*} \approx 300$, thereby concluding no transition takes place in time for reattachment of the boundary layer. This is in line with general observations of Mueller and DeLaurier [23], Lissaman [24], and Carmichael [12] at those Reynolds numbers. Furthermore, the airfoils of the MH showed a laminar separation point relatively far downstream ($x_{ls}/c \approx 0.80$ for the majority of the upper rotor), reducing the possible time (and space) for turbulent transition and subsequent reattachment.

The above determination of the BL state allowed for the proper setup of the CFD simulations to develop the MH rotor model. Figure 8 presents a comparison between the calculated Figure of Merit (FM) and free flight data from JPL's 25-ft. diameter Space Simulator.

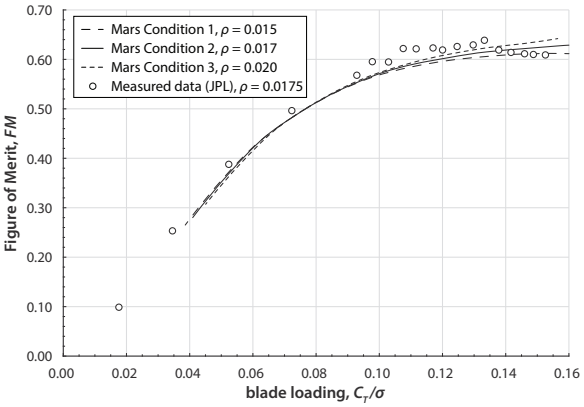

Figure 8. MH rotor Figure of Merit versus blade loading for all Martian Conditions [7]

The measured shaft power was obtained from motor power using a nearly constant motor/drive efficiency of 78%. Evaluation of the effect of the upper rotor wake on transition of the lower rotor boundary layer was not attempted.

COMPUTATIONAL APPROACH

Two-dimensional airfoil sections are analyzed using two-dimensional structured overset grids and solved using the implicit compressible RANS

solver OVERFLOW 2.2n [50]. All solutions presented are run time-accurate in an effort to quantify possible unsteady behavior, and use 6^{th} order central differencing of Euler terms [51] with 2^{nd} order BDF2 time marching.

Airfoil performance is evaluated for average Martian atmospheric conditions, Mars Condition (MC) 2, as previous work showed marginal performance differences with the other variations [7]. Operating conditions for MC 2 are presented in Table 1 and compared to Earth Sea Level Standard (SLS) conditions.

Table 1. Operating conditions for Mars Condition 2 [7]

Variable	Earth SLS	MC 2
Density, ρ [kg/m^3]	1.225	0.017
Temperature, T [K]	288.20	223.20
Gas constant, R [m^2/s^2/K]	287.10	188.90
Specific heat ratio, γ	1.400	1.289
Dynamic viscosity, μ [Ns/m^2]	$1.750 \cdot 10^{-5}$	$1.130 \cdot 10^{-5}$
Static pressure, p [kPa]	101.30	0.72

The (turbulent) Prandtl number is assumed to stay the same as for air. Free stream turbulence and boundary layer receptivity are expected to have a small influence on flat plate performance with sharp leading edges [13], [32], [33], in stark contrast to regular airfoil shapes at low Reynolds numbers. Therefore the free stream turbulence intensity is kept at the standard value $TI \approx 0.082\%$. The influence of compressibility effects is estimated to be small [36], [37] although compressibility is seen to affect the stability of the separated shear layer to some extent.

The angle of attack and Mach number range for each radial station is presented in Table 2. The angle of attack range used 1-degree increments and the Mach range uses increments equal to $M = 0.1$. Each radial station's (M, α) pair provides the lift, drag, and moment coefficients for the C81 airfoil deck files required for the comprehensive analyses. In total, over 3,000 cases are executed on the Pleiades Supercomputer at NASA Ames Research Center.

Table 2. C81 alpha-Mach pair input parameters

CFD station	r/R [~]	α [deg]	M [~]	Re/M [10^{-4}]
Station 1	0.091	-15 to 20	0.10 to 0.30	1.074
Station 2	0.200	-15 to 20	0.10 to 0.40	2.984
Station 3	0.295	-15 to 20	0.10 to 0.50	4.176
Station 4	0.390	-15 to 20	0.10 to 0.50	4.176
Station 5	0.527	-15 to 20	0.20 to 0.50	3.451
Station 6	0.762	-15 to 20	0.20 to 0.70	2.564
Station 7	0.924	-15 to 20	0.20 to 0.85	1.825
Station 8	0.991	-15 to 20	0.20 to 0.90	0.724

TURBULENCE MODELING

Turbulence modeling at very low Reynolds numbers sees some inconsistent conclusions. Kunz and Kroo [52] assumed fully laminar flow at Reynolds numbers up to $Re = 1.2 \cdot 10^4$ for MAV airfoil performance calculations. Winslow *et al.* [15] used the $\gamma Re_{\theta t} - SA$ transition/turbulence model for various airfoils at a similar Reynolds number range. Schmitz indicates that $Re_c \approx 1.0 \cdot 10^4$ is sufficient to trip the shear layer to turbulent flow for a flat plate [11]. Werle showed experimental results for a flat plate at $\alpha = 3°$ and $Re_c \approx 1.0 \cdot 10^4$ with laminar separation and laminar reattachment. A Reynolds number increase to $Re_c \approx 5.0 \cdot 10^4$ showed the transition in the shear layer leading to turbulent reattachment [34], [35].

Even though the intricacies of an LSB may only be truly captured using DNS, several turbulence and transition models using RANS or Large Eddy Simulation (LES) approaches have shown promising results [15], [53]. Some research presents the (expected) advantages of LES over RANS methods in resolving more intricate details of the flow over a flat plate [39], [54], [55], including the possible secondary bubble as found by Crompton [18], albeit all at higher Reynolds numbers than currently under investigation. LES simulations at low Reynolds number and high Mach number are found to be very promising for airfoils tested in work by Anyoji *et al.* [38], but for flat plate-like geometry, some coefficient variations are still observed in work using a DNS approach by Munday *et al.* [56].

The present work uses the Spalart-Allmaras (SA) 1-equation turbulence model [57] (SA-neg-1a) with the Coder 2-equation Amplification Factor Transport (AFT) transition model [58] (SA-AFT2017b). The transition model functions by computing the growth of maximum instability amplitude based on linear stability theory. The SA turbulence model (SA-neg-noft2) with Medida-Baeder 2-equation transition model [59], [60] ($\gamma Re_{\theta t} - SA$) showed similar performance results but is based on a critical Reynolds number and transition length function. Under the current simulation settings, the $\gamma Re_{\theta t} - SA$ model is found to require more time to converge. Because

of the substantial number of cases to be simulated, the SA-AFT2017b model is ultimately preferred.

TIME-ACCURATE SOLVER

All solutions presented are run time-accurate to observe possible unsteady loading. Laitone concludes the superiority of the sharp leading edge in this Reynolds number regime to be through continuous vortex shedding [13]. Pauley *et al.* [20] indicate that 'bubble bursting' is in fact periodic shedding. Time-averaged simulations can therefore manifest a false bubble-like structure in the flowfield. Arena and Mueller [16] also indicate the need for time-accurate results if the flowfield is to be investigated. Differences between averaged and instantaneous flow fields are also presented in experiments using Particle Image Velocimetry (PIV) by Hu and Tamai [61] and LES work by Anyoji *et al.* [38].

Quantification of unsteady behavior of forces for rotor purposes needs to be evaluated, although the monitoring of frequencies and magnitudes of force fluctuations is beyond the scope of the present work. All coefficients are obtained as the mean integrated loads over time for the converged unsteady flowfield. The standard deviations are also obtained.

GEOMETRY DEFINITION

The present work investigates a flat plate and a cambered plate. Some general observations are found in various experiments. The near body grid of the flat plate is shown in Figure 9. The overset grid used to construct the beveled sharp leading edge can be seen in the lower left. The height of the first cell boundary is approximately $10^{-4}c$. The far field limit is set at $50c$. Experimental results indicate decreasing thickness improves performance [31], [62], therefore a low thickness of $t/c = 1\%$ is chosen. It is assumed an MH-sized composite rotor can be sufficiently stiff and strong, in particular the cambered flat plate, as that is expected to have superior performance.

The trailing edge shape is kept blunt as experimental results indicated no influence on performance [13], [33]. The top of the plate is straight, and the bottom is beveled over the front $0.2c$, similar as used in the work by Pelletier and Mueller [33]. The leading edge wedge angle is therefore roughly 3 degrees.

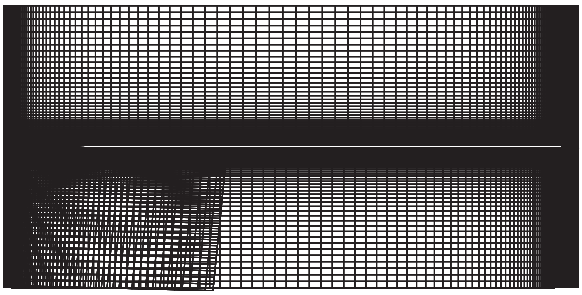

Figure 9. Section of flat plate near-body grid

For the cambered flat plate, $4-6\%$ camber is most beneficial according to experimental work. A camber ratio around $f/c = 5.0\%$ is reported to have the best performance [11], [13], [31], [33]. Forward camber, at $x/c \approx 0.25-0.38$ seems to indicate a performance increase, although only limited and inconclusive data exists [11], [31]. Therefore, maximum camber location is kept at $x/c \approx 0.50$ for this study. Figure 10 shows a section of the near body grid for the 5% cambered plate.

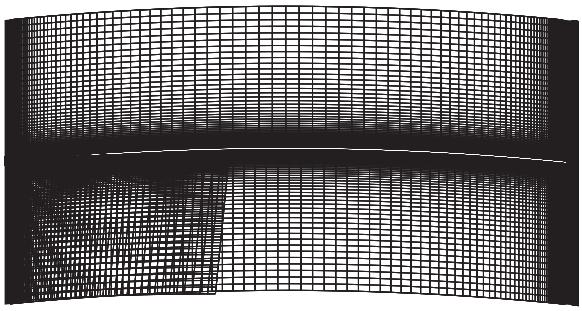

Figure 10. Section of cambered plate near-body grid

Figure 11 shows a comparison of the flat plate, cambered plate, and Mars Helicopter airfoil outboard of $r/R = 0.53$.

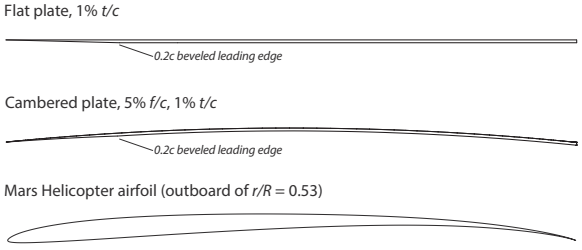

Figure 11. Comparison of plate geometry to Mars Helicopter airfoil

Corrugated airfoils are not considered because they seem to become superior in performance only at still lower Reynolds numbers [24], [31], [32], [61]–[63]. The geometric discontinuities characteristic of those airfoils are likely desirable to delay total flow separation [24]. All validation cases are performed for SLS conditions.

THREE DIMENSIONAL EFFECTS

All simulations performed are two-dimensional. The vast separation at moderate to high angles of attack could yield three-dimensional breakdown of the flow (around $\alpha \approx 8°$ [13], [37], [56]). Modeling vastly separated flow using RANS methods is difficult. Since the majority of the rotor is expected to operate in the 'linear' regime, this is not investigated further at this time.

VALIDATION

The cases present a combination of exotic flow conditions, so validation of the simulation approach is necessary. Low Reynolds number experimental efforts for flat and cambered plates are rare. Several useful sources are referenced [11], [13], [31]–[33], [36], [37], [62]. The very low forces require very accurate equipment, which makes recent work likely to be of higher accuracy.

The low Reynolds number range is prone to strong tunnel interference [64], and there are few references that present two-dimensional coefficients and tunnel interference corrections [33] (this reference is not used because of the substantially higher Reynolds number range). Among the greatest difficulties is the aspect ratio of 'infinite' wings, which can greatly alter airfoil performance. Laitone reports testing a cambered flat plate with $AR = 4$ and $AR = 6$ [13], showing up to 70% change in lift coefficient at higher angles of attack for the higher AR.

FLAT PLATE PERFORMANCE

The flat plate performance of Okamoto *et al.* at $Re_c \approx 1.1 \cdot 10^4 - 1.5 \cdot 10^4$ [32], and Laitone at $Re_c \approx 2.1 \cdot 10^4$ [13] are used to compare two dimensional OVERFLOW computations with three-dimensional experimental results. Laitone used a thin wedge with 1% t/c leading edge and blunt 4% t/c trailing edge. Okamoto *et al.* utilized a 1% t/c flat plate. Both experiments were performed without beveled/sharp leading edges, contrary to OVERFLOW simulations. Figure 12 shows the lift and drag curves versus experiments. The error bars represent the standard deviation (1σ) of the integrated forces for the converged results.

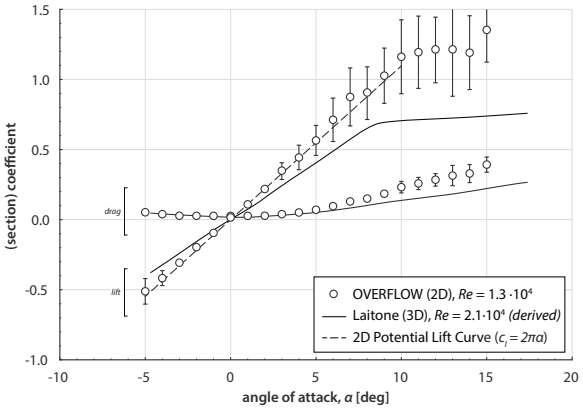

Figure 12. Flat plate lift and drag versus angle of attack for low Reynolds number

The lift and drag curves from Okamoto *et al.* are close to Laitone and are not shown for clarity in Figure 12. Laitone presents only results for positive angles of attack. The negative values are deduced from the inherent symmetry. Figure 13 shows the drag polars from both experimental references. Figure 14 compares the lift to drag ratio versus angle of attack from OVERFLOW with Laitone's results.

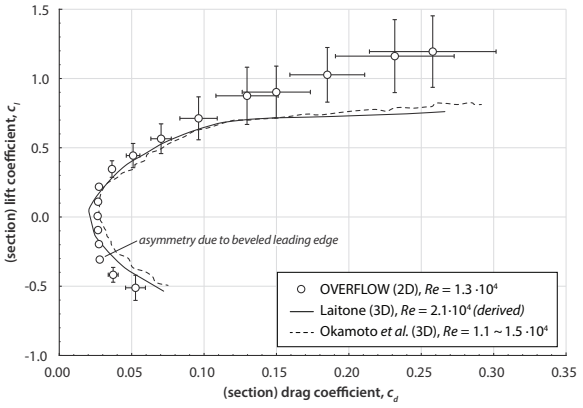

Figure 13. Flat plate drag polar at low Reynolds number

Both the sharp leading edge and the two dimensional nature of the simulations are expected to give rise to higher aerodynamic performance when compared to the experimental data, as can be seen in Figure 13 and Figure 14.

Both Figure 13 and Figure 14 show increased performance of the OVERFLOW results at $\alpha \approx -3.5°$ compared to $\alpha \approx +3.5°$, where the beveled edge is orientated favorably to the incoming flow and results in a local increase in aerodynamic performance.

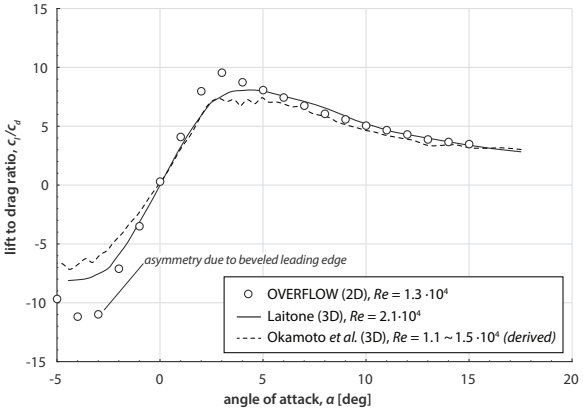

Figure 14. Flat plate lift to drag ratio versus angle of attack at low Reynolds number

CAMBERED PLATE PERFORMANCE

The 5% cambered flat plate performance is also compared to experimental measurements. Laitone used a 5% cambered plate with 1.3% t/c, whereas Okamoto *et al.* used a 6% cambered plate, both 1% thick. Figure 15 shows the lift and drag curves of the cambered plate.

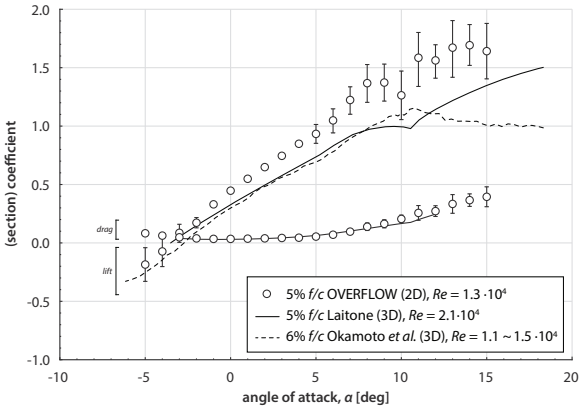

Figure 15. Cambered plate lift and drag versus angle of attack for low Reynolds number

The drag measurements from Okamoto *et al.* in Figure 15 are close to those from Laitone (not displayed for clarity). Both Figure 12 and Figure 15 show the breakdown of the flow for OVERFLOW results around $\alpha = 5°$ where the coefficient fluctuations start to become visible. The 'kink' in the lift curve of Laitone is a local stall effect that only occurs for $AR = 6$ (not for $AR = 4$). Laitone therefore concludes this is a two-dimensional effect that does not occur for low aspect ratios.

Okamoto *et al.*, however, also use $AR = 6$ for their experiments. The lift is seen to vary substantially compared to Laitone, strengthening the argument that measurements and/or tunnel corrections in this Reynolds number range are difficult. Figure 16 shows the drag polar for the cambered plate.

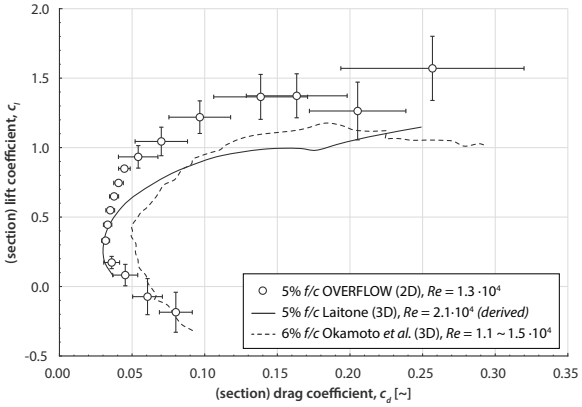

Figure 16. Cambered plate lift and drag versus angle of attack for low Reynolds number

Figure 17 shows the lift to drag ratio comparison. The two dimensional airfoil performance is much higher than three dimensional but coincides at lower and higher angles of attack.

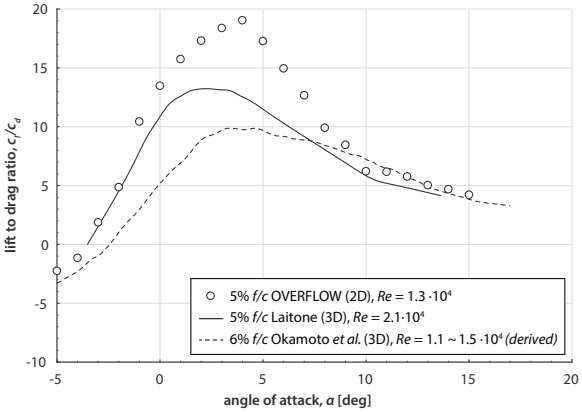

Figure 17. Cambered plate lift to drag ratio versus angle of attack at low Reynolds number

Both the flat plate and cambered plate OVERFLOW simulations show higher performance to three dimensional results; this coincides with the expectations for differences

between two dimensional and three dimensional models.

Compressibility effects are expected to be marginal as shown by experimental work by Suwa *et al.* [36] and Anyoji *et al.* [37] for similar Mach-Reynolds number ranges.

RESULTS

For all (M, α) pairs the lift, drag, and moment coefficient are assembled in C81 format for each radial station to obtain an airfoil performance map. Performance over moderate angles of attack $(-5^\circ \lesssim \alpha \lesssim 5^\circ)$ showed little to no time-based fluctuation in integrated loads. Higher angles of attack showed greater fluctuation in the aerodynamic coefficients. Figure 18 shows convergence of the lift and drag coefficients for the flat plate at high angle of attack. Angles of attack exceeding $\alpha \approx 12^\circ$ are difficult to get to converge.

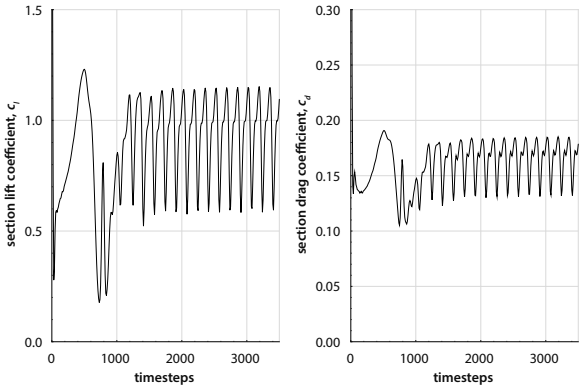

Figure 18. Unsteady force convergence for flat plate at high angle of attack ($\alpha = 8.0^\circ,\ M = 0.20, Re_c \approx 2.0 \cdot 10^3$)

The source of the fluctuations in the integrated loads can be deduced by plotting streamlines near the plate. Figure 19 shows the 'steady' behavior of the flat plate at $\alpha = 5^\circ$.

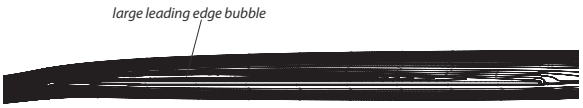

Figure 19. Streamlines for the flat plate showing a steady bubble ($\alpha = 5.0^\circ,\ M = 0.20, Re_c \approx 2.0 \cdot 10^3$)

Upon increasing the angle of attack to $\alpha = 8^\circ$ the leading edge starts to shed vortices, as shown in Figure 20 (and Figure 18).

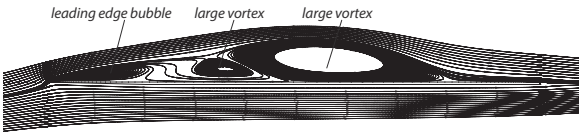

Figure 20. Streamlines for the flat plate showing strong vortex shedding ($\alpha = 8.0^\circ,\ M = 0.20, Re_c \approx 2.0 \cdot 10^3$)

The vortices convect downstream, shed, and eventually dissipate in the wake.

When the streamlines over the cambered plate are plotted for the same angle of attack and Mach number, the leading edge separation is replaced by trailing edge separation, as shown in Figure 21. This partly explains the steadier loads for the cambered plate, and higher performance compared to the flat plate. This flowfield resembles that of the MH airfoil study by Koning *et al.* [7].

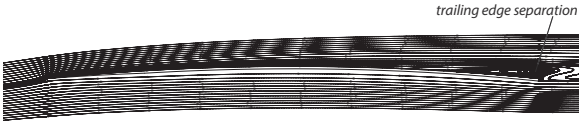

Figure 21. Streamlines for the cambered plate showing trailing edge separation ($\alpha = 8.0^\circ,\ M = 0.20, Re \approx 2.0 \cdot 10^3$)

At sufficiently high angles of attack, vortex shedding occurs naturally on both the flat and cambered plate. It seems that the onset of vortex shedding, during which the vortices are still small and don't grow over the airfoil to the extent as seen in Figure 20, can occur in the 'linear' regime prior to causing severe consequences for the lift and drag coefficient. Figure 22 shows small vortices being shed at $\alpha = 5.0^\circ$, but the airfoil is still operating at a high $c_l/c_d \approx 17.9$, with only minor fluctuations in the converged results.

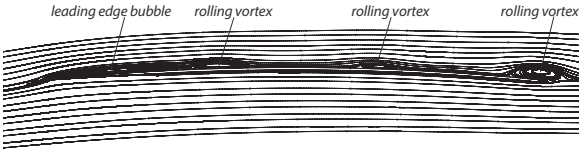

Figure 22. Streamlines for the cambered plate showing discrete shed vortices ($\alpha = 5.0^\circ,\ M = 0.40, Re \approx 1.0 \cdot 10^4$)

Table 3 shows the integrated loads and standard deviation in lift of the airfoil in Figure 22. Two neighboring angles of attack are presented as well to show the airfoil's 'steady' and 'stalled'

operating mode at $\alpha = 4.0°$ and $\alpha = 8.0°$, respectively.

Table 3. Station 6

α [deg]	μ (c_l)	1σ (c_l)	μ (c_d)	c_l/c_d
4.0	0.86	0.0041 (~0.5%)	0.050	17.4
5.0	0.99	0.0253 (~2.5%)	0.056	17.9
8.0	1.35	0.1582 (~12.0%)	0.163	8.3

The complexity of these flows is very high, and the influence of turbulence and transition modeling, differences between two and three dimensional simulations, and inherent limitations in methods used are important to evaluate. Laitone experimentally observed the continuous shedding of vortices and concludes on the superiority of the sharp leading edge for $Re < 4.0 \cdot 10^4$ and $\alpha < 8.0°$: *"(...) The leading edge vortex and the large flow separation region on the upper surface were replaced by a continuous shedding of small vortices that rolled along the upper surface so as to greatly decrease the separated flow"* [13]. This is in line with observations from Figure 22, although at smaller angles of attack the flow seems to reach a steady-like state by means of a separation bubble similar to that shown in Figure 19, as reported by Suwa *et al.* [36] and Anyoji *et al.* [37], [38], and others. Figure 23 shows the computed maximum lift to drag ratio, maximum section lift coefficient, and minimum section drag for all simulated polars on top of the experimental values as presented by McMasters and Henderson [10], shown earlier in Figure 2 and Figure 3. For each radial station and each Mach number, the maximum lift to drag ratio, maximum section lift coefficient, and minimum section drag are obtained from the alpha sweep.

The Reynolds number sensitivity of the flat plate minimum drag coefficients and maximum lift to drag ratio is in agreement with the results of Schmitz [11] and two dimensional laminar flat plate theory.

The cambered plate is seen to obtain a higher lift to drag ratio than the flat plate, despite the unavoidable increase in (minimum) section drag. The scatter in the maximum section lift coefficient data is linked to the inherent difficulties modeling an airfoil near stall.

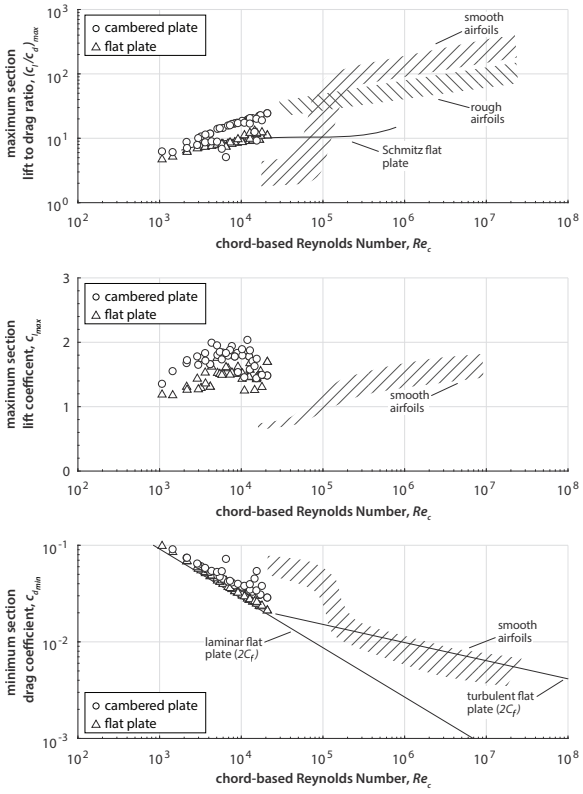

Figure 23. Effects of Reynolds number on computed cambered and flat plate performance (created referring to McMasters and Henderson [10])

CAMRADII ROTOR PERFORMANCE RESULTS

Performance predictions for the flat plate and cambered plate rotor are made using a free-wake analysis in CAMRADII [65]. The coaxial rotor is modeled at the flight conditions for Mars Condition 2 as shown in Table 1. The Mars Helicopter performance is predicted using the rotor model by Koning *et al.* [7]. Figure 24 shows the thrust versus power at 2,800 RPM.

For equal power, the cambered plate is seen to produce around 7% higher thrust compared to the Mars Helicopter rotor in the design thrust range ($C_T = 0.015 - 0.020$).

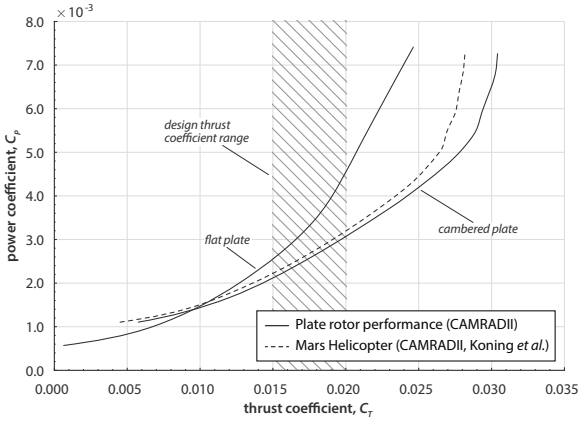

Figure 24. Thrust versus power for $\rho = 0.017\ kg/m^3$, including Mars Helicopter performance from Koning *et al.* [7]

Figure 25 shows the Figure of Merit versus thrust coefficient for the same models.

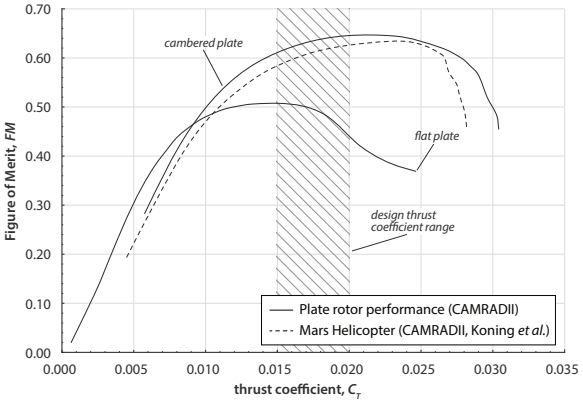

Figure 25. Figure of Merit versus thrust for $\rho = 0.017\ kg/m^3$, including Mars Helicopter performance from Koning *et al.* [7]

The predicted cambered plate Figure of Merit shows an improvement over the Mars Helicopter Figure of Merit prediction of around 5% in the design thrust range.

CONCLUSIONS

The cambered plate rotor model is shown to be competitive with the rotor of the Mars Helicopter for identical twist and chord distribution.

Performance results for the Martian atmosphere show the potential of the cambered plate rotor in both thrust for equal power and Figure of Merit for equal blade loading. The cambered plate airfoil produces 7% greater maximum rotor thrust versus the Mars Helicopter, and 5% higher Figure of Merit over the design thrust coefficient range. Larger maximum thrust allows an increase of design blade loading for the same thrust range for control authority, whereas the larger Figure of Merit reduces power requirements.

The maximum rotor thrust depends on the stall of the airfoil sections. The MH airfoil performance was calculated with the thin-layer Navier-Stokes code C81Gen (ARC2D), the flat and cambered plate results are simulated with the full RANS method OVERFLOW.

Future work will include the analysis of the MH rotor using identical CFD methods, evaluation of the unsteady integrated loads, and a further investigation into the airfoil boundary layer state due to upper-lower rotor interaction and forward flight operation.

ACKNOWLEDGEMENTS

The authors would like to thank William Warmbrodt for his continuing assistance and motivation, Pieter Buning at NASA Langley Research Center for his invaluable help with OVERFLOW, and Pierre-Marie Basset at ONERA for providing essential documentation for the understanding of the flat plate performance.

Michelle Dominquez and Larry Young are thanked for providing (unpublished) preliminary work helping in understanding the performance of flat plates using computational methods. Carl Russell, Alan Wadcock, and Kristen Kallstrom are thanked for their helpful comments and review.

REFERENCES

[1] Lorenz, R. D., "Flight power scaling of airplanes, airships, and helicopters: Application to planetary exploration," *Journal of Aircraft*, vol. 38, no. 2, pp. 208–214, 2001.

[2] Young, L. A., Aiken, E. W., Derby, M., Demblewski, R., and Navarrete, J., "Experimental Investigation and Demonstration of Rotary-Wing Technologies for Flight in the Atmosphere of Mars," in *58th Annual Forum of the AHS International*, 2002.

[3] Balaram, J. (Bob), Canham, T., Duncan, C., Golombek, M., Grip, H. F., Johnson, W., Maki, J., Quon, A., Stern, R., Zhu, D., "Mars Helicopter Technology Demonstrator," in *AIAA Science and Technology Forum and Exposition (AIAA SciTech)*, 2018.

[4] McGee, T., Adams, D., Hibbard, K., Turtle, E., Lorenz, R., Amzajerdian, F., Langelaan, J., "Guidance, Navigation, and Control for Exploration of Titan with the Dragonfly Rotorcraft Lander," in *2018 AIAA Guidance, Navigation, and Control Conference*, 2018, p. 1330.

[5] Balaram, J. and Tokumaru, P. T., "Rotorcrafts for Mars Exploration," in *11th International Planetary Probe Workshop*, 2014.

[6] Grip, H. F., Johnson, W., Malpica, C., Scharf, D. P., Mandić, M., Young, L., Allan, B., Mettler, B., Martin, M. S., "Flight Dynamics of a Mars Helicopter," in *43rd European Rotorcraft Forum*, 2017.

[7] Koning, W. J. F., Johnson, W., and Allan, B. G., "Generation of Mars Helicopter Rotor Model for Comprehensive Analyses," in *Aeromechanics Design for Transformative Vertical Flight*, 2018.

[8] Pines, D. J. and Bohorquez, F., "Challenges facing future micro-air-vehicle development," *Journal of aircraft*, vol. 43, no. 2, pp. 290–305, 2006.

[9] Hoerner, S. F., *Fluid-Dynamic Drag: Practical Information on Aerodynamic Drag and Hydrodynamic Resistance*. Hoerner Fluid Dynamics, 1965.

[10] McMasters, J. and Henderson, M., "Low-speed single-element airfoil synthesis," *Technical Soaring*, vol. 6, no. 2, pp. 1–21, 1980.

[11] Schmitz, F. W., "Aerodynamics of the model airplane. Part 1 - Airfoil measurements," Huntsville, Alabama, 1967.

[12] Carmichael, B. H., "Low Reynolds Number Airfoil Survey, Volume 1," Capistrano Beach, California, 1981.

[13] Laitone, E. V, "Wind tunnel tests of wings at Reynolds numbers below 70 000," *Experiments in Fluids*, vol. 23, no. 5, pp. 405–409, Nov. 1997.

[14] McArthur, J., *Aerodynamics of wings at low Reynolds numbers: boundary layer separation and reattachment*. University of Southern California, 2008.

[15] Winslow, J., Otsuka, H., Govindarajan, B., and Chopra, I., "Basic Understanding of Airfoil Characteristics at Low Reynolds Numbers (104–105)," *Journal of Aircraft*, pp. 1–12, Dec. 2017.

[16] Arena, A. V and Mueller, T. J., "Laminar separation, transition, and turbulent reattachment near the leading edge of airfoils," *AIAA journal*, vol. 18, no. 7, pp. 747–753, 1980.

[17] Alam, M. M., Zhou, Y., Yang, H. X., Guo, H., and Mi, J., "The ultra-low Reynolds number airfoil wake," *Experiments in fluids*, vol. 48, no. 1, pp. 81–103, 2010.

[18] Crompton, M. J., "The thin aerofoil leading edge separation bubble." University of Bristol, 2001.

[19] Gaster, M., *The structure and behaviour of laminar separation bubbles*. HM Stationery Office, 1969.

[20] Pauley, L. L., Moin, P., and Reynolds, W. C., "The structure of two-dimensional separation," *Journal of Fluid Mechanics*, vol. 220, pp. 397–411, 1990.

[21] Mueller, T. J. and Batil, S. M., "Experimental studies of separation on a two-dimensional airfoil at low Reynolds numbers," *AIAA journal*, vol. 20, no. 4, pp. 457–463, 1982.

[22] Wang, S., Zhou, Y., Alam, M. M., and Yang, H., "Turbulent intensity and Reynolds number effects on an airfoil at low Reynolds numbers," *Physics of Fluids*, vol. 26, no. 11, p. 115107, 2014.

[23] Mueller, T. J. and DeLaurier, J. D., "Aerodynamics of Small Vehicles," *Annual Review of Fluid Mechanics*, vol. 35, no. 1, pp. 89–111, Jan. 2003.

[24] Lissaman, P. B. S., "Low-Reynolds-number airfoils," *Annual Review of Fluid Mechanics*, vol. 15, no. 1, pp. 223–239, 1983.

[25] Huang, R. F. and Lin, C. L., "Vortex shedding and shear-layer instability of wing at low-Reynolds numbers," *AIAA Journal*, vol. 33, no. 8, pp. 1398–1403, Aug. 1995.

[26] Obert, E., *Aerodynamic design of transport aircraft*. IOS press, 2009.

[27] Broeren, A. P. and Bragg, M. B., "Unsteady stalling characteristics of thin airfoils at low Reynolds number.," *Progress in Astronautics and Aeronautics*, vol. 195, pp. 191–213, 2001.

[28] Yarusevych, S., Sullivan, P. E., and Kawall, J. G., "On vortex shedding from an airfoil in low-Reynolds-number flows," *Journal of Fluid Mechanics*, vol. 632, p. 245, Aug. 2009.

[29] Liu, H. and Kawachi, K., "Leading-edge vortices of flapping and rotary wings at low Reynolds number.," *Progress in Astronautics and Aeronautics*, vol. 195, pp. 275–285, 2001.

[30] Ellington, C. P. and Usherwood, J. R., "Lift and drag characteristics of rotary and flapping wings.," *Progress in Astronautics and Aeronautics*, vol. 195, pp. 231–248, 2001.

[31] Sunada, S., Sakaguchi, A., and Kawachi, K., "Airfoil section characteristics at a low Reynolds number," *Journal of fluids engineering*, vol. 119, no. 1, pp. 129–135, 1997.

[32] Okamoto, M., Yasuda, K., and Azuma, A., "Aerodynamic characteristics of the wings and body of a dragonfly," *The Journal of Experimental Biology*, vol. 199, no. 2, p. 281 LP-294, Feb. 1996.

[33] Pelletier, A. and Mueller, T. J., "Low Reynolds number aerodynamics of low-aspect-ratio, thin/flat/cambered-plate wings," *Journal of Aircraft*, vol. 37, no. 5, pp. 825–832, 2000.

[34] Werlé, H., *Le tunnel hydrodynamique au service de la recherche aérospatiale*. Office National d'Études et de Recherches Aérospatiales, 1974.

[35] Van Dyke, M. and Van Dyke, M., "An album of fluid motion," 1982.

[36] Suwa, T., Nose, K., Numata, D., Nagai, H., and Asai, K., "Compressibility effects on airfoil aerodynamics at low Reynolds number," in *30th AIAA Applied Aerodynamics Conference*, 2012, p. 3029.

[37] Anyoji, M., Numata, D., Nagai, H., and Asai, K., "Effects of Mach Number and Specific Heat Ratio on Low-Reynolds-Number Airfoil Flows," *AIAA Journal*, vol. 53, no. 6, pp. 1640–1654, Oct. 2014.

[38] Anyoji, M., Nonomura, T., Aono, H., Oyama, A., Fujii, K., Nagai, H., Asai, K., "Computational and experimental analysis of a high-performance airfoil under low-Reynolds-number flow condition," *Journal of Aircraft*, vol. 51, no. 6, pp. 1864–1872, 2014.

[39] Sampaio, L. E. B., Rezende, A. L. T., and Nieckele, A. O., "The challenging case of the turbulent flow around a thin plate wind deflector, and its numerical prediction by LES and RANS models," *Journal of Wind Engineering and Industrial Aerodynamics*, vol. 133, pp. 52–64, 2014.

[40] Smith, A. M. O., "Transition, Pressure Gradient, and Stability Theory.," El Segundo, California, 1956.

[41] Van Ingen, J. L., "A suggested semi-empirical method for the calculation of the boundary layer transition region," *Technische Hogeschool Delft, Vliegtuigbouwkunde, Rapport VTH-74*, 1956.

[42] Bussmann, K. and Ulrich, A., "Systematic Investigations of the Influence of the Shape of the Profile Upon the Position of the Transition Point," Washington, D.C., 1947.

[43] Schlichting, H. and Kestin, J., *Boundary-Layer Theory*, 6th ed. 1968.

[44] Wazzan, A. R., Okamura, T. T., and Smith, A. M. O., "Spatial and Temporal Stability Charts for the Falkner-Skan Boundary-Layer Profiles," 1968.

[45] Owen, P. R. and Klanfer, L., "On the Laminar Boundary Layer Separation from the Leading Edge of a Thin Aerofoil," Aeronautical Research Council London, 1953.

[46] Schubauer, G. B. and Klebanoff, P. S., "Contributions on the mechanics of boundary-layer transition," 1955.

[47] Crabtree, L. F., "Effects of leading-edge separation on thin wings in two-dimensional incompressible flow," *Journal of the Aeronautical Sciences*, vol. 24, no. 8, pp. 597–604, 1957.

[48] Moore, T. W. F., "Some experiments on the reattachment of a laminar boundary layer separating from a rearward facing step on a flat plate aerofoil," *The Aeronautical Journal*, vol. 64, no. 599, pp. 668–672, 1960.

[49] Koning, W. J. F., "Mars Helicopter Rotor Aerodynamics and Modeling," NASA CR-2018-219735, Moffett Field, California, 2018.

[50] Buning, P. and Nichols, R., "User's Manual for OVERFLOW 2.2," *NS Tech. Manual*, 2008.

[51] Pulliam, T., "High order accurate finite-difference methods: as seen in OVERFLOW," in *20th AIAA Computational Fluid Dynamics Conference*, 2011, p. 3851.

[52] Kunz, P. J. and Kroo, I., "Analysis and design of airfoils for use at ultra-low Reynolds numbers," *fixed and flapping wing aerodynamics for micro air vehicle applications*, vol. 195, pp. 35–59, 2001.

[53] Radespiel, R. E., Windte, J., and Scholz, U., "Numerical and experimental flow analysis of moving airfoils with laminar separation bubbles," *AIAA journal*, vol. 45, no. 6, pp. 1346–1356, 2007.

[54] Collie, S., Gerritsen, M., and Jackson, P., "Performance of two-equation turbulence models for flat plate flows with leading edge bubbles," *Journal of Fluids Engineering*, vol. 130, no. 2, p. 21201, 2008.

[55] Rezende, A. L. T. and Nieckele, A. O., "Evaluation Of Turbulence Models To Predict The Edge Separation Bubble Over A Thin Aerofoil," in *Proceedings of the 20 th International Congress of Mechanical Engineering–COBEM*, 2009.

[56] Munday, P. M., Taira, K., Suwa, T., Numata, D., and Asai, K., "Nonlinear lift on a triangular airfoil in low-Reynolds-number compressible flow," *Journal of Aircraft*, vol. 52, no. 3, pp. 924–931, 2014.

[57] Spalart, P. R. and Allmaras, S. R., "A One-Equatlon Turbulence Model for Aerodynamic Flows," *30th Aerospace Sciences Meeting & Exhibit*, p. 23, 1992.

[58] Coder, J. G. and Maughmer, M. D., "Computational fluid dynamics compatible transition modeling using an amplification factor transport equation," *AIAA Journal*, vol. 52, no. 11, pp. 2506–2512, 2014.

[59] Medida, S. and Baeder, J., "Application of the Correlation-based Gamma-Re Theta t Transition Model to the Spalart-Allmaras Turbulence Model," in *20th AIAA Computational Fluid Dynamics Conference*, 2011, p. 3979.

[60] Langtry, R. B. and Menter, F. R., "Correlation-based transition modeling for unstructured parallelized computational fluid dynamics codes," *AIAA journal*, vol. 47, no. 12, pp. 2894–2906, 2009.

[61] Hu, H. and Tamai, M., "Bioinspired corrugated airfoil at low Reynolds numbers," *Journal of Aircraft*, vol. 45, no. 6, pp. 2068–2077, 2008.

[62] Sunada, S., Yasuda, T., Yasuda, K., and Kawachi, K., "Comparison of wing characteristics at an ultralow Reynolds number," *Journal of aircraft*, vol. 39, no. 2, pp. 331–338, 2002.

[63] Kesel, A. B., "Aerodynamic characteristics of dragonfly wing sections compared with technical aerofoils," *Journal of Experimental Biology*, vol. 203, no. 20, pp. 3125–3135, 2000.

[64] West, G. S. and Apelt, C. J., "The effects of tunnel blockage and aspect ratio on the mean flow past a circular cylinder with Reynolds numbers between 10 4 and 10 5," *Journal of Fluid Mechanics*, vol. 114, pp. 361–377, 1982.

[65] Johnson, W., "CAMRAD II Comprehensive Analytical Model of Rotorcraft Aerodynamics and Dynamics." Johnson Aeronautics, Palo Alto, 2005.